Physica Scripta

PAPER

Impact of Ir doping on the thermoelectric transport properties of half-Heusler alloys

RECEIVED
26 June 2024

REVISED
15 August 2024

ACCEPTED FOR PUBLICATION
25 September 2024

PUBLISHED
7 October 2024

B Abdelkebir[1,2], F Semari[1], Z Charifi[2,3,*], H Baaziz[2,3], T Ghellab[2,3], Ş Uğur[4], G Uğur[4] and R Khenata[1,*]

[1] Laboratoire de Physique Quantique de la Matière et de Modélisation Mathématique, Université de Mascara, 29000 Mascara, Algeria
[2] Laboratory of Physics and Chemistry of Materials, University of M'sila, Algeria
[3] Department of Physics, Faculty of Science, University of M'sila, 28000 M'sila, Algeria
[4] Department of Physics, Faculty of Science, Gazi University, 06500 Ankara, Turkey
[*] Authors to whom any correspondence should be addressed.

E-mail: zoulikha@gmail.com, zoulikha.charifi@univ-msila.dz, rabah_khenata@univ-mascara.dz and khenata_rabah@yahoo.fr

Keywords: Half Heusler alloys, Boltzmann, seebeck coefficient, thermoelectric performance

Abstract

Using density functional and and Boltzmann transport theories, we investigate the thermoelectric transport properties $ZrCo_{1-x}$ Ir_x Sb (x = 0, 0.125, 0.25, 0.375, 0.5, 0.625, 0.75, 0.875, 1) half-Heusler alloys. The current work found that increasing the concentration of iridium (Ir_x) from x = 0 to 0.375 in the $ZrCo_{1-x}$ Ir_x Sb alloys from room temperature to 800 K significantly decreased thermal and electrical conductivity due to a shorter relaxation time. Furthermore, our results show that $ZrCo_{0.625}$ $Ir_{0.375}$ Sb has the highest Seebeck coefficient (353.93 μV/K) at 300 K, thereby boosting its thermoelectric performance. Interestingly, the thermoelectric figure of merit (ZT) has exceptional value 1.01 by applying 25% (x = 0.25) of atomic doping of iridium (Ir) with a carrier concentration of $n = 1.47 \cdot 10^{20}$ cm^{-3} at 1000 K and 37.5% (x = 0.375) of atomic doping of iridium (Ir) with a carrier concentration of $n = 7.23 \cdot 10^{19}$ cm^{-3} at 800 K. Calculations present important results on the suitability of the studied alloys for thermoelectric applications.

1. Introduction

Developing methods for converting renewable energy is an efficient solution to address the energy issue, as the world's energy demands are rising, and fossil fuel supplies are running out. Thermoelectric materials are highly beneficial for cooling and heat energy-collecting applications because they are green energy resources. They can directly convert heat energy into electrical energy through the thermoelectric effect.

By utilizing thermoelectric (TE) materials, thermal waste recovery offers a viable approach to generating power that is dependable, sustainable, and expandable through the utilization of waste thermal energy [1, 2]. A thermoelectric device's conversion efficiency is highly dependent on the dimensionless figure of merit ($ZT = S^2\sigma T/k$) of the materials, which S stands for the Seebeck coefficient, σ electrical conductivity, and k thermal conductivity [3]. T indicates the absolute temperature. The two components of thermal conductivity are the electronic contribution (k_e) and the lattice vibration contribution (k_l), where the power factor ($S^2\sigma$) is defined. Nevertheless, the various parameters entering ZT are coupled, so increasing thermoelectric efficiency is not a simple task. Therefore, the task is to find novel compounds and maximize their ZT values by enhancing phonon scattering and maximizing carrier concentration.

Half-Heusler (HH) compounds have garnered significant attention in recent years owing to their thermal stability, high power factor [4–7], cost-effectiveness, and non-toxicity. Research has shown considerable interest in the ZrCoSb and ZrNiSn types of HH alloys. Like other thermoelectric materials, there are two fundamental techniques for boosting the ZT of half-Heusler alloys: lowering their thermal conductivity and raising the power factor. Improving these two TE attributes simultaneously can be difficult because of their relationship. In addition, many other techniques, including point defect scattering [8], nanostructuring [9], phase separation [10], band engineering [11], and plastic deformation, have been used besides carrier concentration optimization to enhance the thermoelectric performance of the half-Heusler compounds. [12]. Highly doped semiconductors

with a carrier concentration of about $10^{18} - 10^{20}$ carriers cm^3 are suitable thermoelectric materials [13]. There are various conceivable combinations for forming HH [14, 15] alloys, including ZrCoSb [16–18] (p-type), TiCoSb [19] (p-type), ZrNiSn [20–24] (n-type), and TiNiSn [25, 26] (n-type), which have been extensively investigated. Although ZT > 1 has already been achieved in n-type HH.

In terms of theory, Yang *et al* [27] estimated the ideal doping concentrations for each of the ternary half-Heusler compounds by computing the electronic transport properties of numerous semiconducting ternary half-Heusler compounds, such as ZrCoSb and TiCoSb, using *ab initio* calculations and the Boltzmann transport equation. Shen *et al* [28] determined the implication of partial nickel substitution with palladium on the thermoelectric properties of ZrNiSn-based half-Heusler compounds and discovered that substituting palladium for nickel leads to a significant, good decrease in thermal conductivity. The study was conducted by Dinesh C. Gupta and Gurunani Bharti [29]. They found that for the CoZrSi and CoZrGe Heusler alloys, the measured ZT values at 900 K are 0.51 and 0.57, respectively. On the other hand, these two authors indicate that half-Heusler alloys based on rhodium have the potential to be used in thermoelectric applications over a wide temperature range [30]. The carrier concentration is optimum at 10^{19} cm^{-3}. In his 2019 paper, D.M. Hoat demonstrated that TaRhSn (Pb) has a higher thermopower than TaRuSb (Bi) because of their denser electronic states close to the Fermi level. With a maximum chemical potential of around −0.25 eV, these materials exhibit a high power factor (PF) in the p-region [31]. According to a theoretical study of the two half-Heusler alloys, KCrSi and KCrGe, carried out by Gurunani *et al* [32], the high figure of merit ZT at 900K is produced by the alloys' poor thermal conductivity and high Seeback coefficient.

On the experimental side, the maximum power factor for TiCoSb-based alloys is $23\mu Wcm^{-1}K^{-2}$ at $850K$, as determined by the experiment [33]. According to estimates from Xia, Yu, *et al* [34] at $300K$, resistivity ρ drops from $\sim 5 \times 10^4 \mu\Omega$ cm in the undoped phase to $1 - 2 \times 10^3 \mu\Omega$ cm in the substituted phases, while the Seebeck coefficient S for ZrCoSb reaches −110 and +130 $\mu V/K$. Mitra, Mousumi, *et al* [35] confirmed experimentally that doping with as little as ~0.3 atomic percent aluminum (Al) can significantly improve the thermoelectric properties of $Hf_{0.3}Zr_{0.7}Co(Sn_{0.3}Sb_{0.7})_{1-x}Al_x$ Half Heusler alloy. $Zr_{1-x}Hf_xCoSb_{0.9}Sn_{0.1}$ alloys are intriguing prospects for mid-temperature power generation applications because of their improved ZT due to Hf-substitution, which has been experimentally accomplished to achieve a very low thermal conductivity (Chauhan *et al* [36]). He *et al*'s research study [37] demonstrates that phonon scattering occurs when Sn substitutes at the Sb sites in half-Heusler compounds ZrCoSb. Regarding the need for a more thorough comprehension of phonon transport for half-Heusler compounds to facilitate further material optimization and improve their thermoelectric performance, this result also holds for a large class of HH compounds, including ZrNiSn, ZrCoBi, and NbFeSb. The thermoelectric performance of the HH compounds is better than that of many current thermoelectric materials.

Using thermoelectric applications to recover electrical energy from waste heat improves the efficiency of heat-to-electricity systems. The need for better-performing, higher-temperature TE materials than those now in use is driving growing interest in this field due to the proposed industrial and military applications of TE materials. In recent years, there has been research on the application of TEs in TE-solar. A few examples of novel use for thermoelectrics (TEs) are biothermal batteries for cardiac pacemakers and radioisotope TE generators for deep-space probe power. Furthermore, TE refrigeration applications include the manufacturing of refrigeration systems, refrigerators, seat coolers for electrically powered cooling and relaxation, and the cooling of electrical components. The TE domain has gained multidisciplinary interest, and the worldwide TE market has risen due to these encouraging developments.

In our previous study, we investigated the structural, electronic, and mechanical properties of $ZrCo_{1-x}Ir_xSb$ half-Heusler alloys across a range of iridium concentrations (x = 0, 0.125, 0.25, 0.375, 0.5, 0.625, 0.75, 0.875, and 1). The findings are published in the article titled *'Iridium's influence on the structural, electronic and mechanical characteristics of* $ZrCo_{1-x}Ir_xSb$ *half-Heusler alloys'* [38]. We evaluated the exchange–correlation (XC) energy using the local density (LDA) and generalized gradient (GGA) approximations. Our findings showed that increasing Ir atom concentration leads to an enlargement of the lattice constant (from 6.10 to 6.36 Å) and bulk modulus (from 138.09 to 149.70 GPa), which result in increased volume and hardness of the compound. The energy band structure was determined using EV-GGA and mBJ-GGA. These methods were employed to improve the accuracy of the band structure and density of states calculations. Our findings indicated that the alloys exhibit semiconductor characteristics with both direct and indirect band gaps, depending on the iridium concentration. Specifically, alloys with x = 0.75 and x = 0.875 exhibited a direct band gap, while other concentrations showed an indirect band gap. The calculated band gap energies were in good agreement with previous theoretical predictions, further validating our approach. Moreover, we computed the elastic constants and determined mechanical stability, bulk modulus, shear modulus, Young's modulus, Poisson's ratio, hardness, anisotropy factor, sound velocities, and Debye temperature using VRH approximations. These results provide a comprehensive understanding of the structural and elastic properties of $ZrCo_{1-x}Ir_xSb$ alloys, supporting their potential for thermoelectric applications.

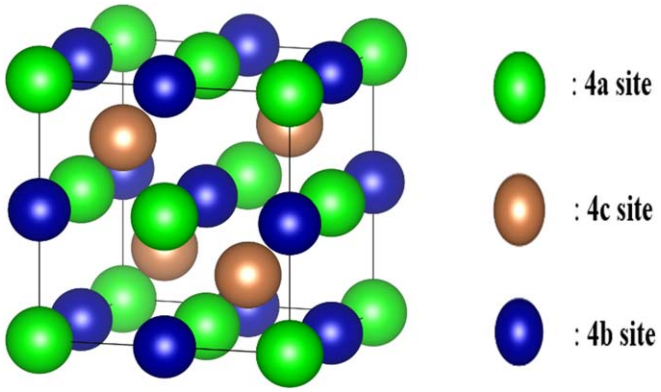

Figure 1. The crystal structure of $C1_b$-type half-Heusler compounds.

Our objective in this work is to investigate the thermoelectric properties of half-Heusler alloys, specifically aiming to identify compounds with a high thermoelectric figure of merit (ZT) and enhanced performance. We focus on varying the concentration of iridium in the $ZrCo_{1-x}Ir_xSb$ (x = 0, 0.125, 0.25, 0.375, 0.5, 0.625, 0.75, 0.875, 1) alloy to achieve this goal.

This study intends to investigate the Boltzmann semiclassical transport equation and constant relaxation time approximation is used to calculate thermoelectric properties, which are implemented in the BoltzTrap code. The Seebeck coefficient, electrical conductivity, thermal conductivity (lattice vibration contribution and electronic contribution), and the figure of merit are calculated versus carrier concentrations at various temperatures. The order of the paper is as follows: The computing process is briefly explained in section 2, and the Boltzmann equation is used to construct the transport coefficients. Section 3 describes the results of $ZrCo_{1-x}Ir_xSb$ (x = 0, 0.125, 0.25, 0.375, 0.5, 0.625, 0.75, 0.875, 1) HH alloys. Finally, section 4 provides a summary of the work's significant findings.

2. Computational details

To achieve the targeted alloy compositions with x values of 0.25, 0.50, 0.75, and 1, we employed a substitution approach where cobalt (Co) atoms were replaced by iridium (Ir) atoms in a unit cell that contains four atoms. Specifically, one, two, three, and four Co sites were substituted with Ir in this configuration. For alloys with x values of 0.125, 0.375, 0.625, and 0.875, the substitution involved one, three, five, and seven Co sites, respectively, within a larger supercell comprising eight atoms. During this process, we accounted for the valence electron configurations of Zr ([Kr] $4d^2\ 5s^2$), Co ([Ar] $3d^7\ 4s^2$), Ir ([Xe] $4f^{14}\ 5d^7\ 6s^2$), and Sb ([Kr] $4d^{10}\ 5s^2\ 5p^3$). The remaining electron configurations were considered as core states.

Figure 1 illustrates the crystal arrangement of C1b-type half-Heusler (HH) alloys, which includes three distinct atomic positions: 4a (0, 0, 0), 4b (0.5, 0), and 4c (0.25, 0.25, 0.25). The crystallographic positions of 4a and 4b can be interchanged. To evaluate this, three structural configurations were analyzed where one of the components occupies the 4c site while the remaining two are situated at the 4a and 4b sites. Lattice parameters for these configurations were optimized using density functional theory (DFT). The stability of these configurations was assessed by comparing their total energies, with the most stable model being the one with the lowest total energy. The DFT calculations were carried out using the WIEN2K software [39]. Band structures were computed employing various methods, including the EV-GGA [40] and mBJ-GGA [41] approximations.

To assess the thermoelectric performance of our material, we calculated the figure of merit (ZT), a key indicator of efficiency in converting thermal energy to electrical energy. This calculation involves several critical transport properties.

We used the semi-classical Boltzmann theory, implemented through the BoltzTraP code [42], to determine the Seebeck coefficient, which measures the voltage generated by a temperature gradient. Electrical conductivity and electronic thermal conductivity were also calculated using the same code, applying a constant relaxation time approximation for consistency [43]. For lattice thermal conductivity, which reflects heat transport via lattice vibrations, we employed Slack's empirical equations and further refined our estimates using the Gibbs2 code [44–47]. This code incorporates thermodynamic parameters such as the Debye temperature and Grüneisen parameter, which are essential for accurate predictions. The total thermal conductivity was computed by summing the electronic and lattice thermal conductivities. This comprehensive value is crucial for evaluating the material's overall thermal performance. The figure of merit (ZT) was then calculated using these properties,

providing a measure of the material's ability to convert waste heat into usable electrical energy. A figure of merit (ZT) is a numerical expression representing the efficiency of a given material. Once all transport coefficients have been obtained, a method to assess the thermoelectric performance of half-Heusler alloys is by calculating the ZT value, which can be expressed as: $ZT = \frac{S^2\sigma T}{k_{tot}}$. The constant relaxation time is taken to be $\tau = 2.10^{-14}$ s, in this equation, the temperature (T) is related to the total thermal conductivity (k_{tot}), which is made up of the sum of the electronic (k_e) and lattice (k_L) thermal conductivity. The Seebeck coefficient (S) and electrical conductivity (σ) are also involved.

3. Results and discussion

3.1. Thermoelectric transport properties

Scientists are driven by the growing need for energy to explore new materials and devices that can efficiently convert thermal energy into electrical power. Materials possessing thermoelectric (TE) properties can be applied in this particular context. These compounds can harness the Seebeck or Peltier phenomenon, which is helpful for generating electrical power. TE materials have a wide range of potential applications in energy devices.

3.1.1. Lattice thermal conductivity

One of a solid's most basic physical properties is its thermal conductivity, which significantly affects a compound's thermal performance. For many years, various theoretical approaches have been used to study the lattice thermal conductivity k_l of semiconductor materials [48–54]. The lattice thermal conductivity k_l refers to the conduction of heat through the vibrations of the lattice ions within a solid. Research into the physics underlying the heat-conduction process has fundamentally enabled a thorough understanding of the nature of lattice vibrations in solids. Weak lattice thermal conductivity is a necessary characteristic for possible thermoelectric materials. The Slacks equation [55, 56] is a commonly used approximation for calculating lattice thermal conductivity:

$$k_l = A \cdot \frac{\overline{M_a}\ {\theta_D}^3 \delta}{\gamma^2\ T\ n^{2/3}} \cdot \tag{1}$$

In which A is a constant having the following value: $A = 3.04 \times 10^{-8}$, $\overline{M_a}$ is the average atomic mass of the crystal, δ^3 is the average volume of just one atom, γ is the Grüneisen parameter, and explicates the crystalline material's anharmonic properties [57], T is the temperature, and n represents the total number of atoms in the primitive unit of a cell.

Since the BoltzraP code computes all transport properties but lattice thermal conductivity k_l (which includes Debye temperature θ_D in its formula), we are forced to apply the Gibbs code to compute Debye temperature θ_D, which is the basis for deriving k_l. Understanding the Gibbs free energy G (x; p; T) is crucial for analyzing the shape and stability of a solid under specific temperature and pressure conditions using the quasi-harmonic approximation. It can be written as

$$G(x;\ p;\ T)\ =\ E(x) + pV(x) + A_{\ vib}(x;\ T)\ . \tag{2}$$

When considering the crystal's total energy $E(x)$, it is essential to consider the variables of the pressure p and the volume $V(x)$. The vibrational Helmholtz free energy is represented by $A_{\ vib}(x;\ T)$. The formula for this is as follows:

$$A_{\ vib}(x;\ T) = \int_0^\infty \left[\frac{\hbar\omega}{2} + K_B T \ln\left(1 - e^{-\frac{\hbar\omega t}{K_B T}}\right)\right] g(x;\ \omega)\, d\omega \tag{3}$$

where K_B Boltzmann's constant $g(x;\ \omega)\, d\omega$ is the phonon density of states. We can mention the vibrational Helmholtz free energy as a function of Debye temperature θ_D by using the Debye model for the phonon density of states, which accounts for the vibrational contribution. It's stated as such:

$$A_{\ vib}(\theta;\ T) = nK_B T \left[\frac{9}{8}\frac{\theta}{T} + 3\ln(1 - e^{-\theta/T}) - D\left(\frac{\theta}{T}\right)\right]. \tag{4}$$

In which $D\left(\frac{\theta}{T}\right)$ denotes the Debye integral, which can be defined as

$$D\left(\frac{\theta}{T}\right) = 3\left(\frac{T}{\theta}\right)^3 \int_0^{\theta/T} \frac{x^3}{e^x - 1}\, dx\ . \tag{5}$$

Table 1. Debye temperature θ_D , The Voulume δ , the average Gruneisen parameter γ and lattice thermal conductivity k_L at 300 K, 600 K, and 900 K for $ZrCo_{1-x}Ir_x$ Sb (x = 0, 0.125, 0.25, 0.375, 0.5, 0.625, 0.75, 0.875, 1) half heusler compounds.

Compounds	T (K)	θ_D (K)	δ $(bohr^3)$	γ	k_L $(W/m.K)$
	T = 300 K	390	388.2395	2.2670522	13.46175
ZrCoSb	T = 600 K	380.2	392.5899	2.2994247	6.08432
	T = 900 K	369.54	397.4335	2.3372204	3.61979
	T = 300 K	383.61	3156.4356	1.9821934	4.47003
$ZrCo_{0.875}$ $Ir_{0.125}$ Sb	T = 600 K	376.56	3185.9342	2.0030573	2.07666
	T = 900 K	369.05	3217.9839	2.02649	1.27753
	T = 300 K	374.24	1609.9521	2.1857597	5.7693
$ZrCo_{0.75}$ $Ir_{0.25}$ Sb	T = 600 K	365.99	1626.3481	2.21286	2.64129
	T = 900 K	357.12	1644.3585	2.2438642	1.59686
	T = 300 K	369.42	3281.2402	2.2703441	3.40421
$ZrCo_{0.625}$ $Ir_{0.375}$ Sb	T = 600 K	360.95	3314.6958	2.29976	1.55257
	T = 900 K	351.82	3351.5454	2.33358	0.93433
	T = 300 K	362.11	830.26	2.18066	9.3408
$ZrCo_{0.5}$ $Ir_{0.5}$ Sb	T = 600 K	354.61	838.2219	2.20598	4.2997
	T = 900 K	346.58	846.9134	2.2347031	2.61674
	T = 300 K	356.93	3379.667	2.2117694	3.60549
$ZrCo_{0.375}$ $Ir_{0.625}$ Sb	T = 600 K	349.54	3411.5779	2.2374263	1.65966
	T = 900 K	341.64	3446.3891	2.2665065	1.01017
	T = 300 K	351.8	1709.459	2.3424518	5.18644
$ZrCo_{0.25}$ $Ir_{0.75}$ Sb	T = 600 K	343.8	1726.2255	2.3728045	2.36646
	T = 900 K	335.19	1744.6459	2.4076051	1.42513
	T = 300 K	347.64	3471.2022	2.2351931	3.61178
$ZrCo_{0.125}$ $Ir_{0.875}$ Sb	T = 600 K	340.67	3502.5922	2.2602781	1.66691
	T = 900 K	333.24	3536.7201	2.2885779	1.01786
	T = 300 K	340.44	439.1815	2.4207408	12.19377
ZrIrSb	T = 600 K	332.45	443.4835	2.45357	5.54466
	T = 900 K	323.83	448.2178	2.49134	3.32524

It is assumed that an isotropic solid is used to compute the Debye temperature.

$$\theta = \frac{\hbar}{K_B}[6\pi^2 V^{1/2} n]^{1/3} f(\sigma)\sqrt{\frac{B_s}{M}} \ . \tag{6}$$

where σ is the Poisson ratio, B_s is the adiabatic bulk modulus, M is the molecular mass per formula unit, and $f(\sigma)$ is determined by

$$f(\sigma) = \left\{3\left[2\left(\frac{2}{3}\frac{1+\sigma}{1-2\sigma}\right)^{3/2} + \left(\left(\frac{1}{3}\frac{1+\sigma}{1-\sigma}\right)^{3/2}\right)\right]^{-1}\right\}^{1/3} . \tag{7}$$

The material exhibits a low lattice thermal conductivity at low Debye temperatures, along with high Grüneisen parameters and volume, as demonstrated in table 1 and figure 2. In figure 2, the lattice thermal conductivity of all HH alloys shows a decreasing trend with temperature. The compound $ZrCo_{0.625}$ $Ir_{0.375}$ Sb exhibits a significantly low value of lattice thermal conductivity. This explains why the Grüneisen parameter of this compound exhibits high values at elevated temperatures. The experimental study was conducted by Bahrami, Amin, *et al* [58]. Half-Heusler compounds demonstrate the potential of cryomilling in decreasing lattice thermal conductivity and enhancing thermoelectric performance by enhancing phonon scattering. The research conducted by Verma, Ajay Kumar, *et al* [59] also highlights the effectiveness of generating significant point defects through heavy isovalent substitution in reducing phonon transport in Half-Heusler alloys. Researchers have demonstrated how manipulating entropy can significantly enhance the thermoelectric performance of an Hf-free half-Heusler compound, resulting in a remarkable reduction in lattice thermal conductivity.

3.1.2. Transport properties

This section will explore the thermoelectric properties of $ZrCo_{1-x}$ Ir_x Sb half Heusler alloys at nine different concentrations, ranging from 0 to 1. All the necessary calculations have been performed to determine the Seebeck coefficient S, electrical conductivity σ, thermal electronic conductivity k_e, and thermoelectric figure of merit ZT. When these parameters are at their optimal values, the dimensionless figure of merit can be maximized. These parameters are interconnected. Therefore, changing just one or two factors will not lead to a

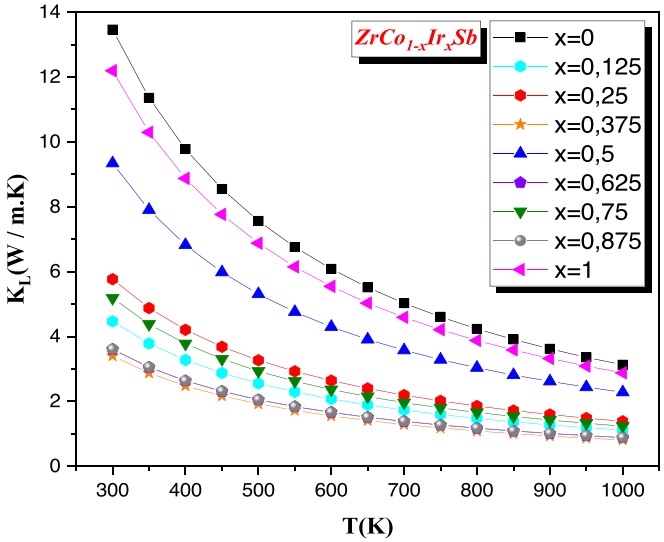

Figure 2. Variations in the lattice thermal conductivity with temperature for $ZrCo_{1-x}Ir_x$ Sb (x = 0, 0.125, 0.25, 0.375, 0.5, 0.625, 0.75, 0.875, 1) HH compounds using mBJ-GGA approximation.

significant increase in value. These properties, calculated from the semi-classical Boltzmann transport equation using the rigid band approximation and constant relaxation time approximation, are sufficient for characterizing a material's efficiency in thermoelectric energy applications [60].

3.1.2.1. Seebeck coefficient

The Seebeck effect and potential difference occur when two dissimilar conductors or semiconductors are brought into contact at different temperatures. This results in the movement of free electrons from the region with a higher temperature to the area with a lower temperature. The electromotive force between these two materials is determined by the temperature difference between the two junctions and the chemical composition of the compounds. Enhanced thermoelectric devices require significant Seebeck coefficients. The Seebeck coefficient measures the magnitude of the thermoelectric effect, which is the generation of an electric voltage in a material due to a temperature difference across it.

$$S = eK_B\sigma^{-1}\sum_k\left(-\frac{\partial f_0}{\partial E}\right)\tau_{\vec{k}}\ v_{\vec{k}}\ v_{\vec{k}}\left(\frac{\varepsilon_k-\mu}{K_BT}\right). \tag{8}$$

where μ the chemical potential ε_k is the band energy.

As seen in figure 3(a), these alloys have Seebeck coefficients greater than 200 μV/K except for composition x = 0.875, whose Seebeck value is higher than 200 μV/K above the temperature of 550 K, and according to other authors' earlier research, high-performance thermoelectric materials are those having a Seebeck coefficient more significant than 200 μV/K [61]. Even at room temperature, we can see that three alloys with concentrations of x = 0.125, x = 0.375, and x = 0.625 have Seebeck coefficients higher than 300 μV/K. Of these, $ZrCo_{0.625}$ $Ir_{0.375}$ Sb it has the highest Seebeck coefficient of 353.93 μV/K, while $ZrCo_{0.875}$ $Ir_{0.125}$ Sb and $ZrCo_{0.375}$ $Ir_{0.625}$ Sb has Seebeck coefficients of 341.13 μV/K and 318.66 μV/K, respectively. Along with these three alloys (x = 0.125, x = 0.375, and x = 0.625), we also observed that for the alloy with concentration x = 0.75, the maximum value S decreases with increasing temperature. Regarding alloys ZrCoSb, $ZrCo_{0.75}$ $Ir_{0.25}$ Sb, $ZrCo_{0.5}$ $Ir_{0.5}$ Sb, and ZrIrSb, the Seebeck value rises with temperature until 600 K, when it achieves its highest value of 235.44 μV/K, 285.57 μV/K, 226.74 μV/K, and 294.95 μV/K, respectively. Above this temperature, the Seebeck values start to drop. Finally, for $ZrCo_{0.125}$ $Ir_{0.875}$ Sb, the Seebeck value increases with increasing temperature until it hits its peak at 800 K, which is 218.87 μV/K, and then begins to fall above this point.

Figure 3(b) presents the Seebeck coefficient (S) as a function of chemical potential for $ZrCo_{1-x}Ir_xSb$ half-Heusler (HH) alloys at a fixed temperature of 900 K. The plot reveals that each alloy exhibits two distinct peaks in the Seebeck coefficient, indicating regions where the thermoelectric performance is particularly enhanced. For the $ZrCo_{0.125}Ir_{0.875}Sb$ alloy, these peaks are most pronounced, with extreme values occurring between 0.12 eV and 0 eV. This behavior suggests significant asymmetry in the density of states around the Fermi level, which in turn affects carrier distribution. The positive peak corresponds to the dominance of holes as the primary charge carriers, while the negative peak reflects the dominance of electrons. The presence of both peaks indicates that

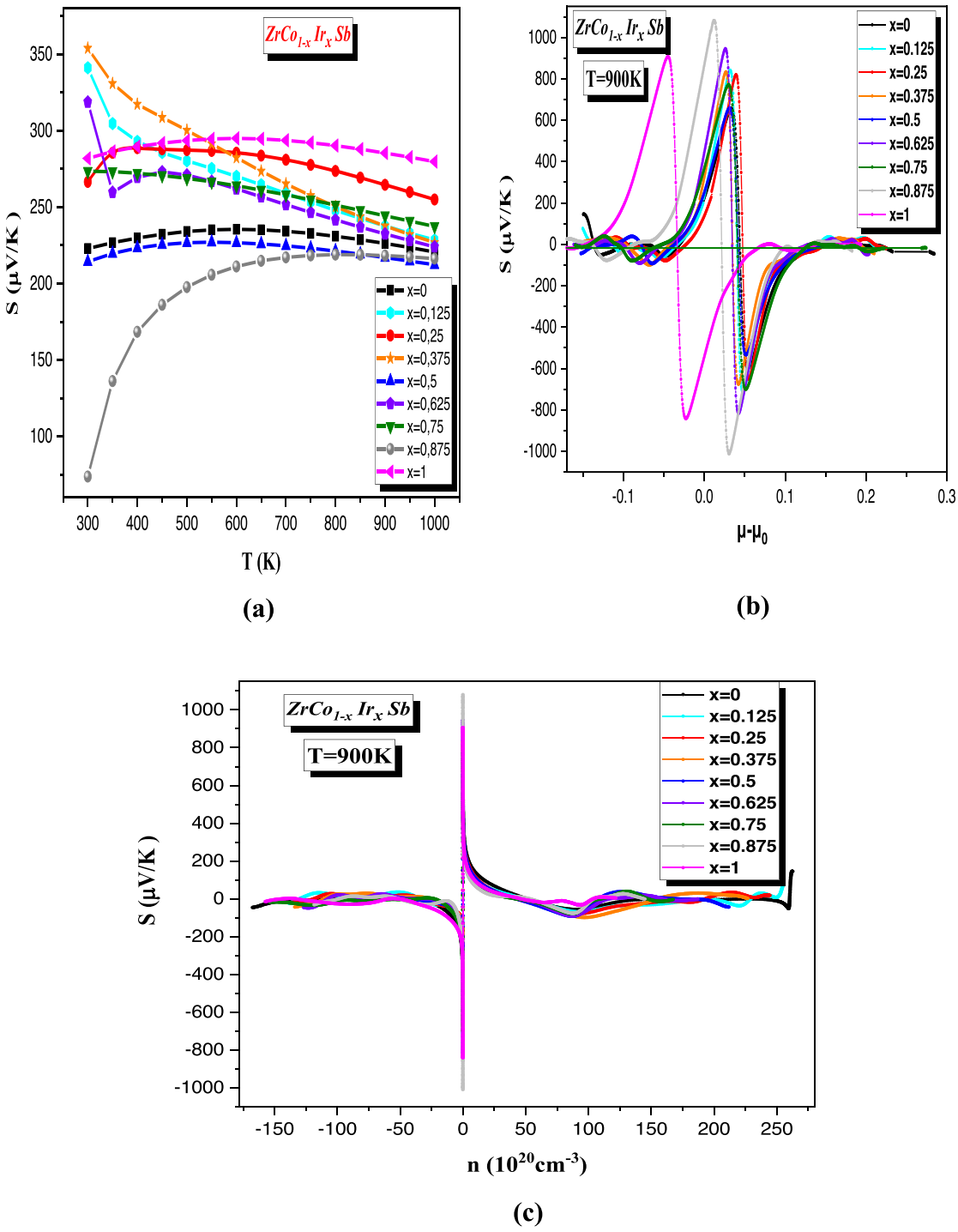

Figure 3. Seebeck coefficients S (μV/K) of $ZrCo_{1-x}Ir_x$ Sb (x = 0, 0.125, 0.25, 0.375, 0.5, 0.625, 0.75, 0.875, 1) HH alloys using mBJ-GGA approximation as a function of (a) temperature, (b) chemical potential at a fixed temperature (T = 900 K) and (c) carrier concentration.

the alloy can be tuned for either p-type or n-type thermoelectric applications depending on the chemical potential, thus offering flexibility in device design.

In figure 3(c), the computed Seebeck coefficients (S) are plotted against carrier concentration at various concentrations and a constant temperature of T = 900 K. The figure clearly shows that for all alloys, the Seebeck coefficient decreases as the carrier concentration increases. This trend is expected, as a higher carrier concentration typically leads to a decrease in the thermoelectric power due to the reduction in the energy difference between the carriers and the Fermi level. However, it is noteworthy that the Seebeck coefficient reaches its maximum value of 1080 μV/K for the $ZrCo_{0.125}Ir_{0.875}Sb$ alloy when the carrier concentration is zero. This maximum value highlights the potential of this alloy for applications requiring high thermoelectric efficiency at low carrier concentrations. Beyond this point, as the carrier concentration increases, the Seebeck

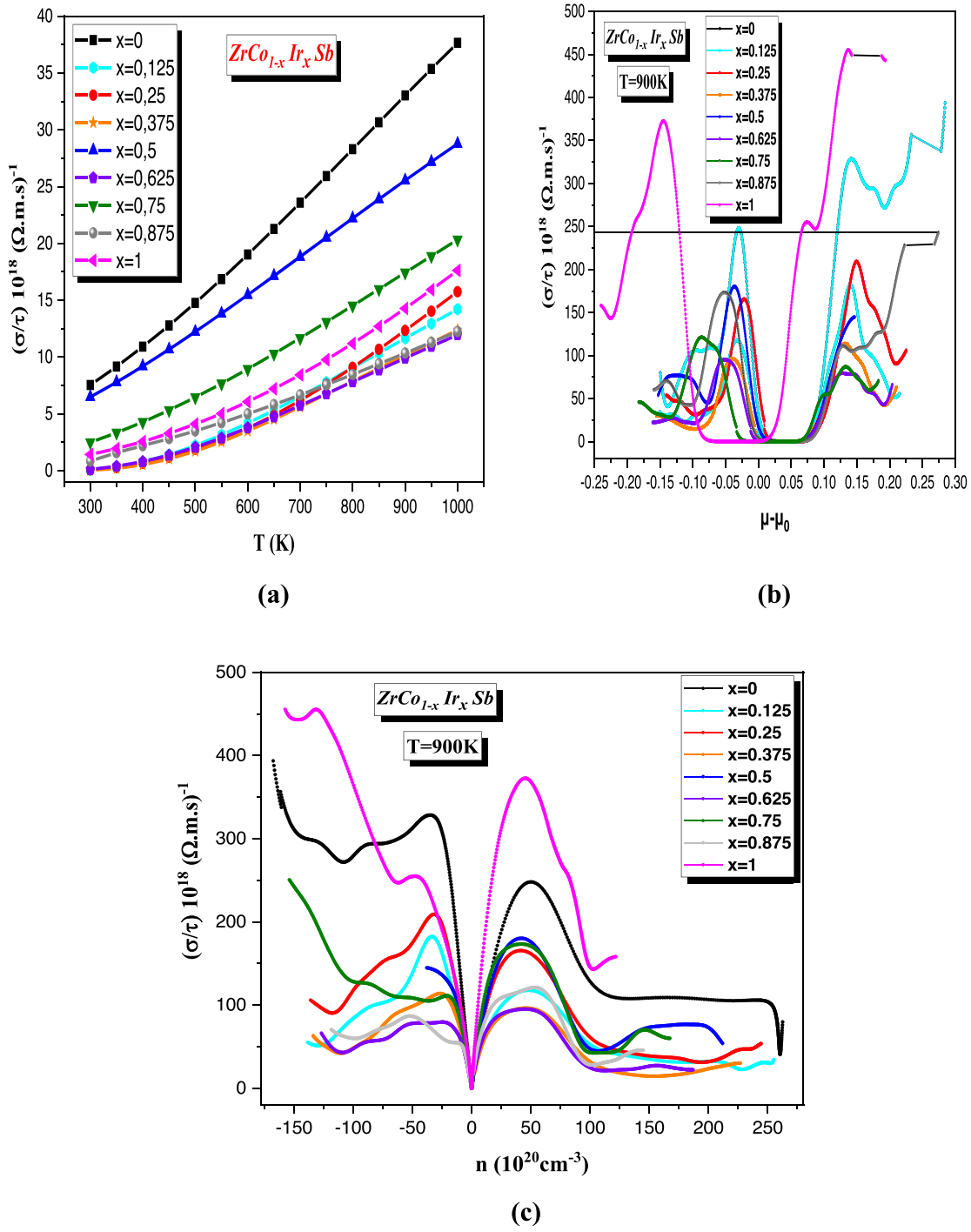

Figure 4. Electrical conductivity $(\sigma/\tau)10^{18}$ $(\Omega.m.s)^{-1}$ of $ZrCo_{1-x}$ Ir_x Sb (x = 0, 0.125, 0.25, 0.375, 0.5, 0.625, 0.75, 0.875, 1) HH alloys using mBJ-GGA approximation as a function of (a) temperature, (b) chemical potential at a fixed temperature (T = 900 K) and (c) carrier concentration.

coefficient begins to decline for all alloys, eventually approaching zero. This decline can be attributed to the increased scattering and lower energy separation between carriers, reducing the ability of the material to maintain a high thermoelectric voltage. The behavior underscores the importance of optimizing carrier concentration to maximize the Seebeck coefficient and, by extension, the thermoelectric performance of the material.

3.1.2.2. Electrical conductivity

The mobility of free charge carriers in a thermoelectric compound generates electrical conductivity due to the thermoelectromotive force; hence, a better thermoelectric material must have a high electrical conductivity that lowers the Joule heating effect [62]. The following expression describes electrical conductivity.

$$\sigma = e^2 \sum_k \left(-\frac{\partial f_0}{\partial E} \right) \tau_{\vec{k}} \, v_{\vec{k}} \, v_{\vec{k}}. \tag{9}$$

where electrical conductivity is denoted by σ, A Fermi distribution function is represented by f_0. $\tau_{\vec{k}}$ and $v_{\vec{k}}$ separately illustrate the relaxation time and group velocity associated with the $\vec{k}$ state.

Plotting the electrical conductivity $(\sigma/\tau)10^{18}$ $(\Omega.\mathrm{m.s})^{-1}$ for $ZrCo_{1-x}Ir_x$ Sb HH alloys (where τ is the relaxation time) with temperature (T) in the range of 300 to 1000 K is shown in figure 4(a). As seen in figure 4(a), the electrical conductivity of all alloys increased linearly with temperature. On the other hand, we found that at room temperature, the electrical conductivity of alloys with concentrations of (x = 0.125, 0.25, 0.375, 0625, and 0.875) is almost null $(\sigma/\tau) \sim 0$). Furthermore, a maximum electrical conductivity value of 37.65×10^{18} $(\Omega.\mathrm{m.s})^{-1}$ at 1000 K was determined for the ternary alloy ZrCoSb, which is higher than the other alloys. Additionally, two maximum values above 20×10^{18} $(\Omega.\mathrm{m.s})^{-1}$ were estimated for $ZrCo_{0.5}Ir_{0.5}$ Sb alloy and $ZrCo_{0.25}Ir_{0.75}$ Sb alloy at the same temperature (1000 K), 28.77×10^{18} $(\Omega.\mathrm{m.s})^{-1}$ and 20.32×10^{18} $(\Omega.\mathrm{m.s})^{-1}$, respectively.

Figure 4(b) illustrates the variation in electrical conductivity (σ/τ) as a function of chemical potential (μ) for $ZrCo_{1-x}Ir_xSb$ half-Heusler (HH) alloys at a constant temperature of 900 K. The figure demonstrates that for all alloys, electrical conductivity increases as the chemical potential moves away from the Fermi level, reaching an optimum value of 372.56×10^{18} $(\Omega\mathrm{m.s})^{-1}$ at a chemical potential of −0.14 eV for the ZrIrSb alloy. This increase suggests an enhanced carrier density or mobility as the chemical potential deepens into the valence band, facilitating greater electrical conductivity. However, as the chemical potential approaches 0 eV, corresponding to the Fermi level, the electrical conductivity sharply declines, reaching a minimum value of 0.00168×10^{18} $(\Omega\mathrm{m.s})^{-1}$, also for the ZrIrSb alloy. At this point, σ/τ effectively becomes zero, indicating that the availability of charge carriers is significantly reduced, as the energy states at the Fermi level are fully occupied in the valence band and only sparsely populated in the conduction band. Beyond the Fermi level, as the chemical potential continues to rise, electrical conductivity begins to increase again, reflecting the thermal excitation of electrons into the conduction band, which restores the material's conductivity. This behavior highlights the complex interplay between chemical potential and electronic structure in determining the electrical properties of these alloys, suggesting that fine-tuning the chemical potential could be key to optimizing electrical performance for thermoelectric applications.

Figure 4(c) depicts the variation in electrical conductivity (σ/τ) as a function of carrier concentration for the $ZrCo_{1-x}Ir_xSb$ HH alloys. The plot shows that the ZrIrSb alloy exhibits the highest electrical conductivity at a carrier concentration of 45.81×10^{20} cm^{-3} in the negative carrier concentration region. This indicates that at this particular concentration, the alloy's charge carriers are optimally positioned within the band structure to facilitate maximum electrical transport. However, as the carrier concentration approaches the Fermi level, the electrical conductivity for all alloys decreases, eventually reaching zero. This reduction is likely due to increased scattering and reduced mobility as carrier concentration increases, particularly near the Fermi level where the balance between available states and carrier energy levels is most delicate. The observed decline to zero conductivity at the Fermi level further underscores the importance of carrier concentration in controlling the material's electrical properties. These insights provide a valuable framework for optimizing doping levels and engineering the electronic structure to achieve desirable electrical conductivity, especially for enhancing the thermoelectric efficiency of these materials.

3.1.2.3. Electronic thermal conductivity

k_e, the electronic thermal conductivity, is a measure of the heat current that occurs when there is a temperature difference. To create a more advanced material for thermoelectric technology, it is essential to have low thermal conductivity. The electronic contribution to thermal conductivity can be described as follows:

$$k_e = K_B^2 T \sum_k \left(-\frac{\partial f_0}{\partial E} \right) \tau_{\vec{k}} \, v_{\vec{k}} \, v_{\vec{k}} \left(\frac{\varepsilon_k - \mu}{K_B T} \right)^2 - T\sigma S^2 \, . \tag{10}$$

We also use the Wiedemann–Franz law [63] to determine the electronic thermal conductivity:

$$k_e = \mathcal{L} \mathrm{T} \sigma. \tag{11}$$

The Lorenz number is represented by $\mathcal{L}$. However, $\mathcal{L}$ certain semiconductor thermoelectric materials with heavy doping are extremely near the degenerate limit [65].

Figure 5(a) displays the electronic thermal conductivities (k_e/τ) of 10^{14} W $(\mathrm{K.m.s})^{-1}$ for $ZrCo_{1-x}Ir_x$ Sb HH alloys throughout a temperature range of 300–1000 K. This figure also shows that k_e/τ for all HH alloys increases with temperature. On the flip side, we observed that the electronic thermal conductivity of almost all alloys—aside from alloys ZrCoSb $ZrCo_{0.5}Ir_{0.5}$ Sb is practically null at room temperature ($(k_e/\tau) \sim 0$). Furthermore, the $ZrCo_{0.625}Ir_{0.375}$ Sb alloy was found to have a lower minimum electronic thermal conductivity

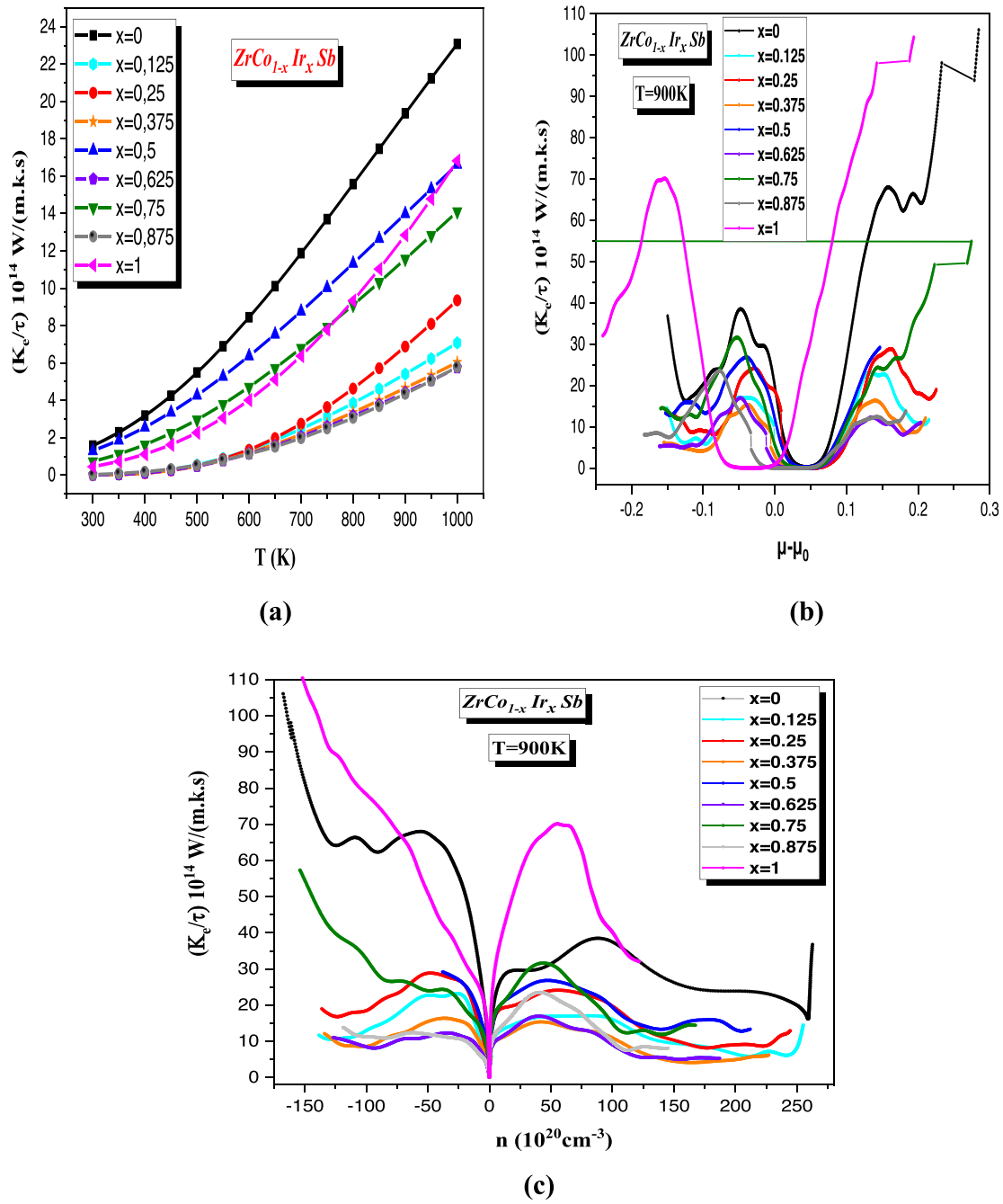

Figure 5. Electronic thermal conductivities (k_e/τ) of 10^{14} W (K.m.s)$^{-1}$ of $ZrCo_{1-x}Ir_x$ Sb (x = 0, 0.125, 0.25, 0.375, 0.5, 0.625, 0.75, 0.875, 1) HH alloys using mBJ-GGA approximation as a function of (a) temperature, (b) chemical potential at a fixed temperature (T = 900 K) and (c) carrier concentration..

value 0.002 × 10^{14} W (K.m.s)$^{-1}$ at 300 K than other alloys, which assists in clarifying why it has the highest thermoelectric performance. In addition, the alloys with concentrations of (x = 0.125, 0.25, 0.375, 0625, and 0.875) exhibit the lowest electronic thermal conductivity at high temperatures (1000 K), ranging from 5.74 to 9.34 × 10^{14} W (K.m.s)$^{-1}$. This further highlights the alloys' high thermoelectric performance.

Figure 5(b) illustrates the variation in electronic thermal conductivity (κ_e/τ) as a function of chemical potential (μ) for the $ZrCo_{1-x}Ir_xSb$ half-Heusler (HH) alloys at a fixed temperature of 900 K. The graph shows a characteristic trend where κ_e/τ increases with chemical potential across all alloys, reaching a minimal value of 0.018×10^{14} W(K·ms)$^{-1}$ at −0.03 eV for the ZrIrSb alloy. This point marks a region where the thermal transport due to electrons is nearly suppressed, likely due to the low density of states available for conduction near this chemical potential. As μ approaches 0 eV, corresponding to the Fermi level, κ_e/τ becomes nearly zero, indicating the minimal contribution of electronic carriers to thermal conductivity at this energy level. Beyond this, as μ continues to rise, κ_e/τ starts to increase again, reflecting the enhanced thermal transport as more charge carriers are thermally excited into higher energy states. The plot reaches an optimum value of

Table 2. The estimated values of S, k_{total} and ZT of $ZrCo_{1-x}Ir_xSb$ HH alloys at temperatures of 300, 600, and 900 using EV-GGA and mBJ-GGA approximations.

x	T (K)	EV-GGA			mBJ-GGA			Previous calculations		
		S $(\mu V/K)$	k_{total} $(W/m.K)$	ZT	S $(\mu V/K)$	k_{total} $(W/m.K)$	ZT	S $(\mu V/K)$	k_{total} $(W/m.K)$	ZT
0	T = 300	210	16.75	0.13	222	16.60	0.12	130 [34]	22 [9]	0.12 [30]
	T = 600	227	22.94	0.54	235	22.97	0.55	—	—	—
	T = 900	221	41.89	0.70	226	42.34	0.71	—	—	—
0.125	T = 300	211	4.48	0.01	341	4.47	∼0			
	T = 600	263	4.52	0.72	270	4.75	0.77			
	T = 900	236	11.29	0.96	237	12.09	0.97			
0.25	T = 300	266	5.75	∼0	266	5.77	∼0			
	T = 600	290	4.84	0.61	285	5.33	0.68			
	T = 900	273	13.80	1	264	15.35	1.01			
0.375	T = 300	302	3.40	∼0	353	3.40	∼0			
	T = 600	287	3.57	0.79	280	3.92	0.84			
	T = 900	244	9.42	1	237	10.25	1			
0.5	T = 300	233	11.54	0.13	214	11.92	0.14			
	T = 600	237	15.97	0.56	226	17.04	0.56			
	T = 900	225	29.13	0.71	217	30.58	0.7			
0.625	T = 300	235	3.62	0.02	318	3.67	∼0			
	T = 600	256	3.98	0.78	261	15.34	0.2			
	T = 900	289	9.80	0.97	232	53.97	0.17			
0.75	T = 300	211	7.35	0.19	273	6.63	0.16			
	T = 600	232	13.79	0.61	263	11.78	0.63			
	T = 900	223	27.63	0.73	244	24.55	0.76			
0.875	T = 300	57	3.65	∼0	73	3.65	∼0			
	T = 600	214	3.73	0.66	211	3.91	0.68			
	T = 900	221	9.20	0.91	218	9.71	0.91			
1	T = 300	276	13.04	0.04	281	13.08	0.05	34.4 [65]	9.5 [65]	—
	T = 600	291	13.98	0.44	294	13.56	0.46	—	—	—
	T = 900	285	27.52	0.71	285	29.01	0.72	—	—	—

70.09×10^{14} W(K·ms)$^{-1}$ at a chemical potential of −0.15 eV for the ZrIrSb alloy, indicating that at this particular energy level, the balance between the number of carriers and their ability to transport thermal energy is maximized. This behavior highlights the sensitive dependence of electronic thermal conductivity on the position of the chemical potential within the electronic band structure, suggesting potential for fine-tuning κ_e/τ through precise control of doping and carrier concentration to enhance thermoelectric performance.

Figure 5(c) presents the variation of electronic thermal conductivity (κ_e/τ) as a function of carrier concentration for the $ZrCo_{1-x}Ir_xSb$ HH alloys. The plot reveals that the electronic thermal conductivity decreases with increasing carrier concentration for all alloys, reaching its lowest point when the carrier concentration is zero. This trend suggests that at low carrier concentrations, the reduced number of available charge carriers limits the material's ability to conduct heat via electronic means. However, as the carrier concentration continues to increase, κ_e/τ begins to rise again, indicating that a higher density of charge carriers can effectively contribute to the thermal conductivity of the material. Notably, the ZrIrSb alloy achieves an optimum value of 115.55×10^{14} W(K·ms)$^{-1}$ at a carrier concentration of -157.47×10^{20} cm^{-3}. This peak value underscores the importance of optimizing carrier concentration to balance electrical and thermal transport properties, which is critical for maximizing the thermoelectric efficiency of the alloy. The observed trends highlight the delicate interplay between carrier concentration and electronic thermal conductivity, suggesting that careful tuning of these parameters can lead to significant improvements in thermoelectric performance.

3.1.2.4. Figure of merit

ZT values around or more prominent than unity are regarded as having good properties for materials used in thermoelectric devices [64, 65]. Table 2 shows that the $ZrCo_{1-x}Ir_xSb$ HH alloys' calculated figure of merit ZT from x = 0 to x = 1 using the modified Beck-Johnson approximation (mBJ-GGA) agrees well with the previous calculations [31–34]. Figures 6(a)–(d)–(e) illustrates that a maximum ZT of approximately 1.01 was attained $ZrCo_{0.75}Ir_{0.25}Sb$ at 1000 K with a carrier concentration of $n = 1.47 \cdot 10^{20}$ cm^{-3} and $ZrCo_{0.625}Ir_{0.375}Sb$ at 800 K with a carrier concentration of $n = 7.23 \cdot 10^{19}$ cm^{-3}. This is attributed to the greater Seebeck coefficient

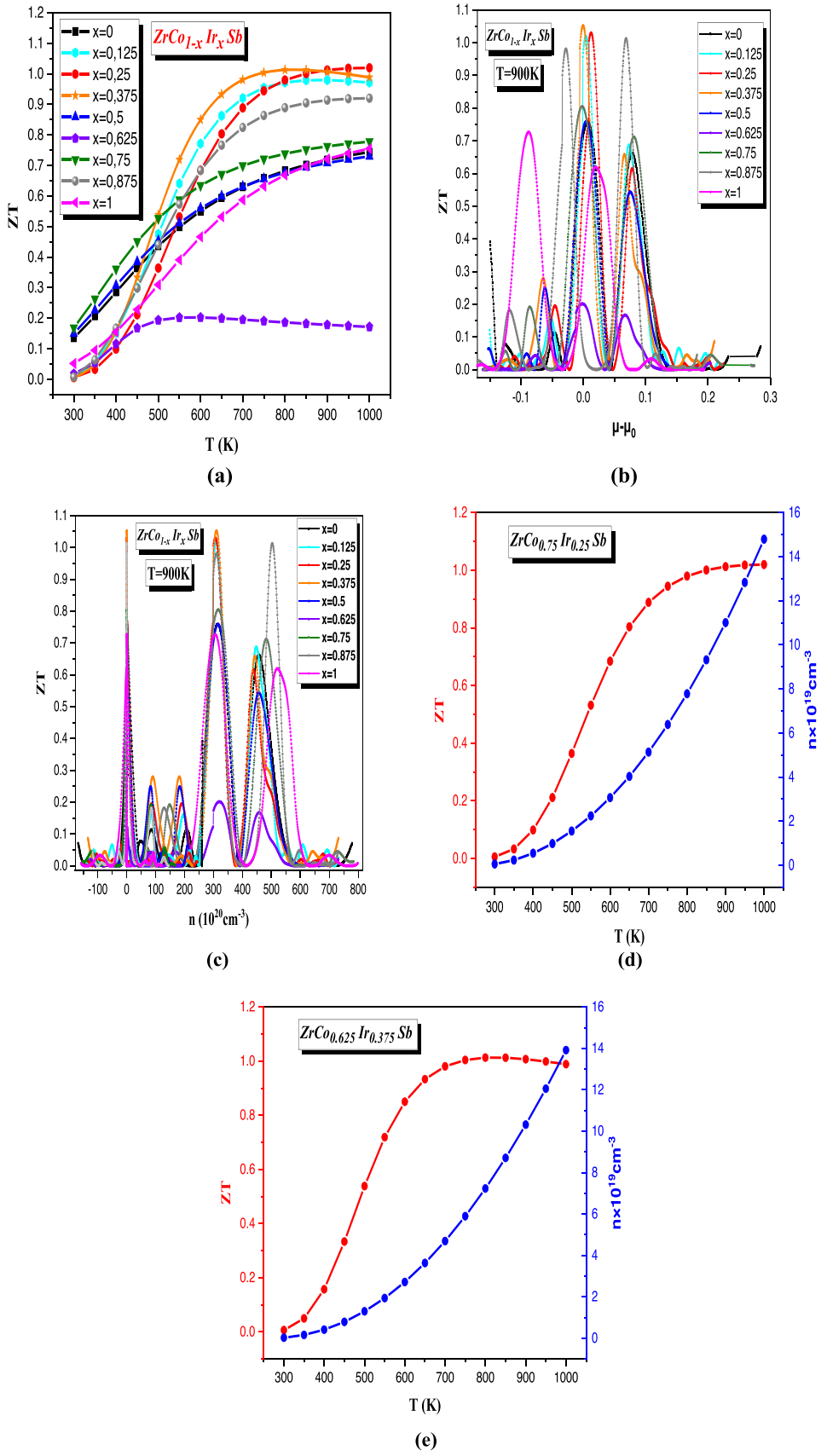

Figure 6. Figure of merit of $ZrCo_{1-x}$ Ir_x Sb (x = 0, 0.125, 0.25, 0.375, 0.5, 0.625, 0.75, 0.875, 1) HH alloys using mBJ-GGA approximation as a function of (a) temperature, (b) chemical potential at a fixed temperature (T = 900 K), (c) carrier concentration. temperature and carrier concentration (d) for $ZrCo_{0.75}$ $Ir_{0.25}$ Sb and (e) for $ZrCo_{0.625}$ $Ir_{0.375}$ Sb HH.

values and lower thermal conductivity, as shown in table 2. These findings highlight the latest advancements in HH alloys and surpass the previously documented results for trenary HH alloy [66–76]. It is worth mentioning that in figure 6(a), the increase in HH alloys is more pronounced at higher temperatures. Except for $ZrCo_{1-x}$ Ir_x Sb alloys at concentrations of x = 0.125, x = 0.375, and x = 0.625, the value decreases at 950, 850, and 650, respectively. Nevertheless, according to table 2, the values for $ZrCo_{1-x}$ Ir_x Sb (x = 0.125, 0.25, 0.375, 0.625, and 0.875) at room temperature are extremely close to zero. Based on this table, the concentration of $ZrCo_{0.375}$ $Ir_{0.625}$ Sb in the alloy is deficient. The value is less than 0.2. In our earlier publications, we have also computed the *ZT* values for various thermoelectric materials and provided a detailed analysis of the results. [77–79].

Figures 6(b) and (c) illustrate the variations in the thermoelectric figure of merit (ZT) as functions of chemical potential (μ) and carrier concentration for the $ZrCo_{1-x}Ir_xSb$ half-Heusler (HH) alloys at a fixed temperature of 900 K. These figures reveal the nuanced relationship between the ZT values and the electronic structure of the alloys, demonstrating their potential as high-temperature thermoelectric semiconductors.

In figure 6(b), the ZT values are plotted against the chemical potential. The graph shows that the ZT value fluctuates as the chemical potential shifts, reflecting the complex interplay between electrical conductivity, Seebeck coefficient, and thermal conductivity within the material. Notably, the $ZrCo_{0.625}Ir_{0.375}Sb$ alloy achieves a peak ZT value of 1.05 at a chemical potential of -5.62×10^{-4} eV. This peak indicates an optimal balance where the electronic properties align to maximize the efficiency of thermoelectric conversion. The location of this peak suggests that even slight adjustments to the chemical potential can significantly impact the thermoelectric performance, emphasizing the need for precise control over doping levels and electronic structure.

Figure 6(c) presents the ZT values as a function of carrier concentration. As seen in the figure, the ZT values exhibit a similar sensitivity to carrier concentration, with the $ZrCo_{0.625}Ir_{0.375}Sb$ alloy again standing out, reaching its maximum ZT value of 1.05 at a carrier concentration of 0.43×10^{20} cm^{-3}. This peak suggests that an optimal carrier concentration exists where the thermoelectric performance is maximized. The ZT value's dependency on carrier concentration highlights the importance of achieving the right balance between carrier mobility and density, which is crucial for enhancing thermoelectric efficiency.

These findings indicate that the $ZrCo_{0.625}Ir_{0.375}Sb$ alloy has a particularly favorable combination of electronic and thermal properties that make it well-suited for high-temperature thermoelectric applications. The ability to fine-tune ZT through adjustments to chemical potential and carrier concentration offers valuable insights into the design and optimization of thermoelectric materials, paving the way for more efficient energy conversion technologies.

4. Conclusion

The thermoelectric transport properties of $ZrCo_{1-x}$ Ir_x Sb (x = 0, 0.125, 0.25, 0.375, 0.5, 0.625, 0.75, 0.875, 1) half-Heusler alloys with varying compositions were analyzed using the DFT and Boltzmann transport theories. The overall thermal conductivity closely aligns with the findings from previous calculations. It was discovered that by increasing the concentration of iridium (Ir_x) from x = 0 to 0.375 in the $ZrCo_{1-x}$ Ir_x Sb alloys from room temperature to 800 K, there was a notable decrease in thermal and electrical conductivity. This can be attributed to a shorter relaxation time. In order to enhance the thermoelectric performance, decrease in thermal conductivity is crucial for efficient thermoelectric generators. In addition, this work demonstrates that this particular material $ZrCo_{0.625}$ $Ir_{0.375}$ Sb exhibits the highest Seebeck coefficient (353.93 $\mu V/K$) at 300 K, which significantly enhances its thermoelectric capabilities. Finally, there is a significant increase $ZrCo_{1-x}$ Ir_x Sb for the extensively researched half-Heusler alloys, surpassing the previous maximum for ZrMSb (M = Co or Ir) ternary alloys of 0.74 or higher. Unexpectedly, we accomplished a substantial increase in thermoelectric properties with a *ZT* value of 1.01 by applying 25% (x = 0.25) of atomic doping of iridium (Ir) with a carrier concentration of $n = 1.47 \cdot 10^{20}$ cm^{-3} 1000 K and 37.5% (x = 0.375) of atomic doping of iridium (Ir) with a carrier concentration of $n = 7.23 \cdot 10^{19}$ cm^{-3} at 800 K. Consequently, we trust that these alloys will make excellent thermoelectric application candidates.

The investigation of $ZrCo_{1-x}Ir_xSb$ half-Heusler alloys and their thermoelectric properties presents significant potential for practical applications in various fields. The alloys studied, particularly with x = 0.25, demonstrate a high thermoelectric figure of merit (ZT) of 1.01 at 1000 K. This promising performance underscores the suitability of these materials for several key applications:

1. **Waste heat recovery:** These alloys can effectively convert waste heat from industrial processes, automotive exhausts, and power generation systems into electrical energy. This application is crucial for improving energy efficiency and reducing greenhouse gas emissions by harnessing otherwise wasted thermal energy.

2. **Power generation:** In remote or off-grid locations, where conventional power sources may be limited, these materials can be utilized in thermoelectric generators to provide a reliable source of electricity by exploiting temperature gradients.
3. **Cooling systems:** The efficiency of these alloys in thermoelectric applications also extends to cooling technologies. Their ability to manage and dissipate heat makes them suitable for cooling electronics, refrigeration systems, and air conditioning units, offering a solid-state alternative to traditional cooling methods.
4. **Wearable electronics:** The capability to convert body heat into electrical energy presents opportunities for powering wearable devices and sensors. This advancement can contribute to the development of innovative health monitoring systems and enhance the functionality of IoT-enabled wearable technologies.

By showcasing the broad range of applications enabled by the thermoelectric properties of $ZrCo_{1-x}Ir_xSb$ alloys, this work emphasizes the material's potential impact on energy efficiency, power generation, thermal management, and wearable technology.

Acknowledgments

All authors would like to thank the general directorate for scientific research and technological development for their financial support during the realization of this work.

Data availability statement

All data that support the findings of this study are included within the article (and any supplementary files).

ORCID iDs

Z Charifi https://orcid.org/0000-0003-3875-4716
H Baaziz https://orcid.org/0000-0003-4860-2740
R Khenata https://orcid.org/0000-0002-5573-1711

References

[1] Bell L E 2008 Cooling, heating, generating power, and recovering waste heat with thermoelectric systems *Science* **321** 1457–61
[2] LeBlanc S 2014 Thermoelectric generators : linking material properties and systems engineering for waste heat recovery applications *Sustainable Materials and Technologies 1* 26–35
[3] Snyder G J and Toberer E S 2008 Complex thermoelectric materials *Nat. Mater.* **7** 105–14
[4] He J and Tritt T M 2017 Advances in thermoelectric materials research: Looking back and moving forward *Science* **357** eaak 9997
[5] Poon S J 2019 Half Heusler compounds: promising materials for mid-to-high temperature thermoelectric conversion *J. Phys.* D **52** 493001
[6] Naydenov G A *et al* 2019 Huge power factor in p-type half-Heusler alloys NbFeSb and TaFeSb *Journal of physics: Materials* **2** 035002
[7] Chen S and Ren Z 2013 Recent progress of half-Heusler for moderate temperature thermoelectric applications *Mater. Today* **16** 387–95
[8] Yang J, Meisner G P and Chen L 2004 Strain field fluctuation effects on lattice thermal conductivity of ZrNiSn-based thermoelectric compounds *Appl. Phys. Lett.* **85** 1140–2
[9] Xie W *et al* 2012 Recent advances in nanostructured thermoelectric half-Heusler compounds *Nanomaterials* **2** 379–412
[10] Schwall M and Balke B 2013 Phase separation as a key to a thermoelectric high efficiency *Phys. Chem. Chem. Phys.* **15** 1868–72
[11] Fu C *et al* 2015 Band engineering of high performance p-type FeNbSb based half-Heusler thermoelectric materials for figure of merit $zT > 1$ *Energy & Environmental Science* **8** 216–20
[12] Rogl G *et al* 2020 Half-Heusler alloys: enhancement of ZT after severe plastic deformation (ultra-low thermal conductivity) *Acta Mater.* **183** 285–300
[13] (ed) 2010 *Materials for Sustainable Energy : A Collection of Peer-Reviewed Research and Review Articles from Nature Publishing Group* (World Scientific)
[14] Graf T, Felser C and Parkin S S P 2011 Simple rules for the understanding of Heusler compounds *Prog. Solid State Chem.* **39** 1–50
[15] Bos J-W G and Downie R A 2014 Half-Heusler thermoelectrics: a complex class of materials *J. Phys. Condens. Matter* **26** 433201
[16] Chauhan N S *et al* 2016 A synergistic combination of atomic scale structural engineering and panoscopic approach in p-type ZrCoSb-based half-Heusler thermoelectric materials for achieving high ZT *J. Mater. Chem.* C **4** 5766–78
[17] Yan X *et al* 2013 Thermoelectric property study of nanostructured p-type half-Heuslers (Hf, Zr, Ti) CoSb0. 8Sn0. 2 *Adv. Energy Mater.* **3** 1195–200
[18] Chauhan N S *et al* 2018 Facile fabrication of p-and n-type half-Heusler alloys with enhanced thermoelectric performance and low specific contact resistance employing spark plasma sintering *Mater. Lett.* **228** 250–3
[19] Yan X *et al* 2012 Stronger phonon scattering by larger differences in atomic mass and size in p-type half-Heuslers Hf 1− x Ti x CoSb 0.8 Sn 0.2 *Energy Environ. Sci.* **5** 7543–8

[20] Chauhan N S *et al* 2018 Vanadium-doping-induced resonant energy levels for the enhancement of thermoelectric performance in Hf-free ZrNiSn half-Heusler alloys *ACS Appl. Energy Mater.* **1** 757–64
[21] Chen S *et al* 2013 Effect of Hf concentration on thermoelectric properties of nanostructured n-type half-heusler materials HfxZr1–xNiSn0. 99Sb0. 01 *Adv. Energy Mater.* **3** 1210–4
[22] Bhardwaj A *et al* 2015 Panoscopically optimized thermoelectric performance of a half-Heusler/full-Heusler based *in situ* bulk composite Zr 0.7 Hf 0.3 Ni 1+ x Sn: an energy and time efficient way *Phys. Chem. Chem. Phys.* **17** 30090–101
[23] Chauhan N S *et al* 2018 A nanocomposite approach for enhancement of thermoelectric performance in Hafnium-free Half-Heuslers *Materialia* **1** 168–74
[24] Chauhan N S *et al* 2018 Compositional tuning of ZrNiSn half-Heusler alloys: thermoelectric characteristics and performance analysis *J. Phys. Chem. Solids* **123** 105–12
[25] Bhattacharya S *et al* 2000 Effect of Sb doping on the thermoelectric properties of Ti-based half-Heusler compounds, TiNiSn 1 − x Sb x *Appl. Phys. Lett.* **77** 2476–8
[26] Misra D K *et al* 2015 Enhanced power factor and reduced thermal conductivity of a half-Heusler derivative Ti9Ni7Sn8: a bulk nanocomposite thermoelectric material *Appl. Phys. Lett.* **106**
[27] Yang J *et al* 2008 Evaluation of half-Heusler compounds as thermoelectric materials based on the calculated electrical transport properties *Adv. Funct. Mater.* **18** 2880–8
[28] Shen Q *et al* 2001 Effects of partial substitution of Ni by Pd on the thermoelectric properties of ZrNiSn-based half-Heusler compounds *Appl. Phys. Lett.* **79** 4165–7
[29] Gurunani B and Gupta D C 2023 Exploring the electronic structure, mechanical behaviour, thermal and high-temperature thermoelectric response of CoZrSi and CoZrGe Heusler alloys *Sci. Rep.* **13** 22834
[30] Gurunani B and Gupta D C 2024 Exploring the multifaceted properties: structural, electronic, magnetic, mechanical, thermodynamic, transport, and optical characteristics of rhodium-based half-Heusler alloys *J. Mater. Sci.* **59** 12502–25
[31] Hoat D M 2019 Electronic structure and thermoelectric properties of Ta-based half-Heusler compounds with 18 valence electrons *Comput. Mater. Sci.* **159** 470–7
[32] Gurunani B, Ghosh S and Gupta D C 2024 Comprehensive investigation of half Heusler alloy: unveiling structural, electronic, magnetic, mechanical, thermodynamic, and transport properties *Intermetallics* **170** 108311
[33] Wu T *et al* 2007 Thermoelectric properties of p-type Fe-doped TiCoSb half-Heusler compounds *J. Appl. Phys.* **102**
[34] Xia *et al* 2000 Thermoelectric properties of semimetallic (Zr, Hf) CoSb half-Heusler phases *J. Appl. Phys.* **88** 1952–5
[35] Mitra M *et al* 2022 Conventional Half-Heusler alloys advance state-of-the-art thermoelectric properties *Mater. Today Phys.* **28** 100900
[36] Chauhan N S *et al* 2019 Enhanced thermoelectric performance in p-type ZrCoSb based half-Heusler alloys employing nanostructuring and compositional modulation *Journal of Materiomics* **5** 94–102
[37] He R *et al* 2020 Unveiling the phonon scattering mechanisms in half-Heusler thermoelectric compounds *Energy Environ. Sci.* **13** 5165–76
[38] Abdelkebir B, Charifi Z, Baaziz H, Ghellab T, Khenata R and Bin-Omran S 2024 Iridium's influence on the structural, electronic and mechanical characteristics of ZrCo1-xIrxSb half-heusler alloys, *Physica* B **688** 416166
[39] Blaha P *et al* 2019 WIEN2k: An augmented plane wave plus local orbitals program for calculating crystal properties *Materials Science and Engineering* (Techn. Universitat) http://susi.theochem.tuwien.ac.at/reg_user/textbooks/usersguide.pdf
[40] Engel E and Vosko S H 1993 *Phys. Rev.* B **47** 20
[41] Becke A D and Johnson E R 2006 *A Simple e_ective Potential for Exchange* (American Institute of Physics)
[42] Tran F and Blaha P 2009 Accurate band gaps of semiconductors and insulators with a semilocal exchange-correlation potential *Phys. Rev. Lett.* **102** 226401
[43] Madsen G K H and Singh D J 2006 BoltzTraP. A code for calculating band-structure dependent quantities *Comput. Phys. Commun.* **175** 67–71
[44] Blanco M A, Francisco E and Luana V G I B B S 2004 GIBBS : isothermal-isobaric thermodynamics of solids from energy curves using a quasi-harmonic Debye model *Comput. Phys. Commun.* **158** 57–72
[45] Toher C *et al* 2014 High-throughput computational screening of thermal conductivity, Debye temperature, and Grüneisen parameter using a quasiharmonic Debye model *Physical Review* B **90** 174107
[46] Blanco M A *et al* 1996 Thermodynamical properties of solids from microscopic theory: applications to MgF2 and Al2O3 *J. Mol. Struct. Theochem.* **368** 245–55
[47] Poirier J-P 2000 *Introduction to the Physics of the Earth's Interior.* (Cambridge University Press)
[48] Klemens P G 1951 The thermal conductivity of dielectric solids at low temperatures (theoretical) *Proceedings of the Royal Society of London. Series A. Mathematical and Physical Sciences* **208** 108–33
[49] Callaway J 1959 Model for lattice thermal conductivity at low temperatures *Phys. Rev.* **113** 1046
[50] Asen-Palmer M *et al* 1997 Thermal conductivity of germanium crystals with different isotopic compositions *Physical review* B **56** 9431
[51] Ladd A J C, Moran B and Hoover W G 1986 Lattice thermal conductivity: a comparison of molecular dynamics and anharmonic lattice dynamics *Physical Review* B **34** 5058
[52] Turney J E *et al* 2009 Predicting phonon properties and thermal conductivity from anharmonic lattice dynamics calculations and molecular dynamics simulations *Physical Review* B **79** 064301
[53] Omini M and Sparavigna A 1996 Beyond the isotropic-model approximation in the theory of thermal conductivity *Phys. Rev.* B **53** 9064
[54] Broido D A, Ward A and Mingo N 2005 Lattice thermal conductivity of silicon from empirical interatomic potentials *Phys. Rev.* B **72** 014308
[55] Slack G A 1973 Nonmetallic crystals with high thermal conductivity *J. Phys. Chem. Solids* **34** 321–35
[56] Shinde S L and Goela J 2006 *Condens. Matter Phys. XVIII* **271** 133
[57] Nandanpawar M and Rajagopalan S 1982 Grüneisen numbers in hexagonal crystals *J. Acoust. Soc. Am.* **71** 1469–72
[58] Bahrami A *et al* 2021 Reduced lattice thermal conductivity for half-Heusler ZrNiSn through cryogenic mechanical alloying *ACS Appl. Mater. Interfaces* **13** 38561–8
[59] Verma A K *et al* 2023 Approaching the minimum lattice thermal conductivity in TiCoSb half-Heusler alloys by intensified point-defect phonon scattering *Materials Advances* **4** 6655–64
[60] Zhang X *et al* 2023 Ultralow lattice thermal conductivity and improved thermoelectric performance in a Hf-free half-Heusler compound modulated by entropy engineering *J. Mater. Chem.* A **11** 8150–61
[61] Chaput L *et al* 2005 Transport in doped skutterudites : *ab initio* electronic structure calculations *Physical Review* B **72** 085126
[62] Feng Z *et al* 2019 Electronic structure as a guide in screening for potential thermoelectrics : Demonstration for half-Heusler compounds *Phys. Rev.* B **100** 085202

[63] Aliabad et al 2012 Ab initio calculations of structural, optical and thermoelectric properties for CoSb3 and ACo4Sb12 (A = La, Tl and Y) compounds Comput. Mater. Sci. 65 509–19
[64] Kim H-S et al 2015 Characterization of Lorenz number with Seebeck coefficient measurement APL Mater. 3
[65] Rabina O, Lin Y-M and Dresselhaus M S 2001 Anomalously high thermoelectric figure of merit in Bi 1− x Sb x nanowires by carrier pocket alignment Appl. Phys. Lett. 79 81–3
[66] Takeuchi T 2009 Conditions of electronic structure to obtain large dimensionless figure of merit for developing practical thermoelectric materials Mater. Trans. 50 2359–65
[67] Yadav K et al 2021 Optical phonon mode assisted thermal conductivity in p-type ZrIrSb Half-Heusler alloy : a combined experimental and computational study J. Phys. D 54 495303
[68] Sekimoto T et al 2007 High-thermoelectric figure of merit realized in p-type half-Heusler compounds : ZrCoSnxSb1-x Jpn. J. Appl. Phys. 46 L673
[69] Culp S R et al 2008 '(Zr, Hf) Co (Sb, Sn) half-Heusler phases as high-temperature (>700 °C) p-type thermoelectric materials Appl. Phys. Lett. 93 022105
[70] Maji P et al 2010 Effects of Rh on the thermoelectric performance of the p-type Zr0. 5Hf0. 5Co1− xRhxSb0. 99Sn0. 01 Half-Heusler alloys J. Solid State Chem. 183 1120–6
[71] Yuan B et al 2017 Effects of Sb substitution by Sn on the thermoelectric properties of ZrCoSb J. Electron. Mater. 46 3076–82
[72] He R et al 2014 Investigating the thermoelectric properties of p-type half-Heusler Hf x (ZrTi) 1− x CoSb 0.8 Sn 0.2 by reducing Hf concentration for power generation Rsc Advances 4 64711–6
[73] Yan X et al 2011 Enhanced thermoelectric figure of merit of p-type half-Heuslers Nano Lett. 11 556–60
[74] Rausch E et al 2015 Fine tuning of thermoelectric performance in phase-separated half-Heusler compounds J. Mater. Chem. C 3 10409–14
[75] Ghellab T, Baaziz H, Charifi Z, Telfah M, Alsaad A, Telfah A, Hergenroder R and Sabirianov R 2022 Mater. Sci. Semicond. Process. 141 106415
[76] Telfah A, Ghellab T, Baaziz H, Charifi Z, Alsaad A M and Sabirianov R 2022 J. Magn. Magn. Mater. 562 169822
[77] Charifi Z, Ghellab T, Baaziz H and Soyalp F 2022 Int. J. Energy Res. 46 13855–73
[78] Ghellab T, Baaziz H, Charifi Z and Latelli H 2023 Physica B 653 414678
[79] Ghellab T, Charifi Z and Baaziz H 2024 Mater. Sci. Semicond. Process. 172 108048